AGU PUBLICATIONS

JGR

Journal of Geophysical Research: Planets

RESEARCH ARTICLE
10.1002/2015JE004943

Key Points:
- Tidal elongation from orbital decay produces surface stresses
- These stresses align with the observed grooves on the surface, implying a connection to tides
- Our model implies that Phobos' interior is weak with a stronger elastic outer layer

Correspondence to:
T. A. Hurford,
terry.a.hurford@nasa.gov

Citation:
Hurford, T. A., E. Asphaug, J. N. Spitale, D. Hemingway, A. R. Rhoden, W. G. Henning, B. G. Bills, S. A. Kattenhorn, and M. Walker (2016), Tidal disruption of Phobos as the cause of surface fractures, *J. Geophys. Res. Planets*, *121*, 1054–1065, doi:10.1002/2015JE004943.

Received 21 SEP 2015
Accepted 20 MAY 2016
Accepted article online 27 MAY 2016
Published online 22 JUN 2016

Tidal disruption of Phobos as the cause of surface fractures

T. A. Hurford[1], E. Asphaug[2], J. N. Spitale[3], D. Hemingway[4], A. R. Rhoden[2,5], W. G. Henning[1,6], B. G. Bills[7], S. A. Kattenhorn[8], and M. Walker[9]

[1]NASA Goddard Space Flight Center, Greenbelt, Maryland, USA, [2]School of Earth and Space Exploration, Arizona State University, Tempe, Arizona, USA, [3]Planetary Science Institute, Tucson, Arizona, USA, [4]Department of Earth and Planetary Sciences, University of California, Santa Cruz, Santa Cruz, California, USA, [5]Johns Hopkins Applied Physics Laboratory, Laurel, Maryland, USA, [6]Center for Research and Exploration in Space Science and Technology, University of Maryland, College Park, Maryland, USA, [7]Jet Propulsion Laboratory, California Institute of Technology, Pasadena, California, USA, [8]Department of Geological Sciences, University of Alaska Anchorage, Anchorage, Alaska, USA, [9]Earth, Planetary, and Space Sciences, University of California, Los Angeles, Los Angeles, California, USA

Abstract Phobos, the innermost satellite of Mars, displays an extensive system of grooves that are mostly symmetric about its sub-Mars point. Phobos is steadily spiraling inward due to the tides it raises on Mars lagging behind Phobos' orbital position and will suffer tidal disruption before colliding with Mars in a few tens of millions of years. We calculate the surface stress field of the deorbiting satellite and show that the first signs of tidal disruption are already present on its surface. Most of Phobos' prominent grooves have an excellent correlation with computed stress orientations. The model requires a weak interior that has very low rigidity on the tidal evolution time scale, overlain by an ~10–100 m exterior shell that has elastic properties similar to lunar regolith as described by Horvath et al. (1980).

1. Introduction

Phobos' global network of ~10–100 m wide, kilometers-long linear features ("grooves") can be seen in Figure 1. Some resemble pit chains or graben while others resemble secondary crater chains (catenae). Some appear to radiate from the largest crater, ~9 km Stickney [*Thomas et al.*, 1979]; however, most grooves have no geometric relationship to Stickney, indicating that they did not form because of that impact event. Differing morphologies suggest that either a range of evolutionary progression or more than one mechanism is responsible for groove formation. Parallel grooves overprint all of Phobos' major craters, including Stickney, crossing their ejecta deposits, implying that groove formation postdates major crater formation and takes place in regolith.

Phobos' bulk density $\rho_{av} = 1880$ kg/m^3 and semimajor axis $a = 9376$ km place it significantly inside the Roche limit (3.19 R_{Mars}) of Mars for a fluid body [*Witasse et al.*, 2014; *Dobrovolskis*, 1982]. The limited available spectroscopy reveals a generally asteroid-like surface composition with little, if any, evidence of hydration [*Pieters et al.*, 2014; *Rivkin et al.*, 2002]. Details of the global surface geomorphology at the scale of groove formation are unknown; the best images from Mars orbiters are a few meters/pixel locally but do not provide global coverage [*Basilevsky et al.*, 2014]. Thermal inertia indicates that the surface is mostly powder to ~0.1–1 m depth and may extend much deeper [*Lunine et al.*, 1982]. On the Moon, the powdery regolith is hypothesized to behave seismically as a uniform elastic layer to depths of ~100 m [*Horvath et al.*, 1980], perhaps analogous to Phobos.

Many of Phobos' grooves feature pit chains. Several mechanisms have been suggested for their formation, such as thin ejecta sheets from Mars [*Murray and Heggie*, 2014], cohesionless regolith draining into dilated fractures [*Horstman and Melosh*, 1989], gas jets, or boulders bouncing downhill [*Wilson and Head*, 1989]. While some pitted grooves resemble secondary ejecta chains, or catenae, there is no suitable source crater on Mars or on Phobos. Moreover, a relationship to major Martian craters would imply that the grooves are billions of years old, contradicting observations of their relative geologic youthfulness.

Phobos' orbit decays due to the tides it raises on Mars lagging behind Phobos' orbital position [*Kaula*, 1964; *Mignard*, 1981; *Dobrovolskis*, 1982; *Burns*, 1978; *Bills et al.*, 2005] and shortly after the Viking spacecraft obtained the first geomorphic images of Phobos, it was proposed that stresses from orbital decay cause grooves [*Soter and Harris*, 1977]. But, assuming an internally homogeneous Phobos, it proved impossible to account for the buildup of failure stress in the exterior regardless of the value assumed for Phobos' rigidity

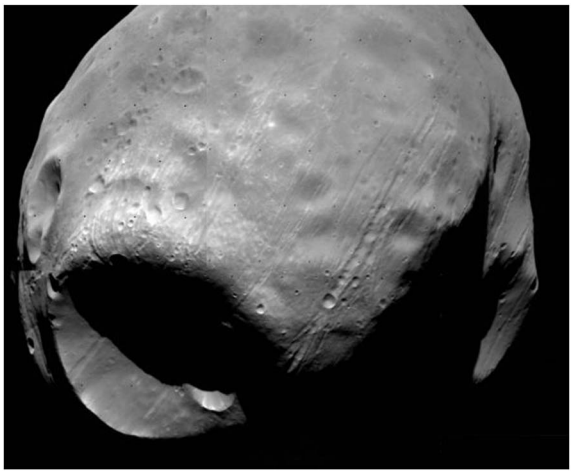

Figure 1. Phobos' surface is covered with parallel linear features and pit/crater chains, collectively called grooves. Stickney crater is shown in the lower left of the image. Phobos has a triaxial shape of 13.0 km × 11.4 km × 9.1 km in radius. Image Credit: Viking Project, Jet Propulsion Laboratory, NASA.

(see Appendix A). Also, stress from orbital decay follows a $1/a^3$ dependency, where a is the semimajor axis (currently 2.77 R_{Mars}, decaying at ~2 m per century). Hence, the greatest tidal stress would have built up most recently, whereas the geological record shows that the most prominent grooves range in ages and are not always the youngest features [*Weidenschilling*, 1979]. Therefore, the tidal model languished. Here we revisit the tidal origin of surface fractures with a more detailed treatment that shows the production of significant stress in a surface layer, with a very strong correlation to the geometry of grooves.

2. Tidal Stress and Groove Orientations

Tidal theory is built on the assumption that undeformed planets are spherical bodies and that their tidal deformation is small compared to their radii [*Sabadini and Vermeersen*, 2004]. In Phobos' case (13.0 km × 11.4 km × 9.1 km in radius), the long and short axes deviate from a sphere by ~20% [*Willner et al.*, 2014]. The tide-raising potential acting on Phobos can be written as an expansion of Legendre polynomials [*Sabadini and Vermeersen*, 2004]. The lowest-order term is a second-order Legendre polynomial and is the tide-raising potential of a spherical body with average radius. We assume that perturbations on the tide-raising potential due to Phobos' irregular shape are accounted for by higher-order Legendre polynomial terms. For this study, the resulting tidal deformation from gravitational terms higher than second order are assumed to be small. We also assume that stresses due to the formation of Phobos' irregular shape have relaxed away prior to any successive tidal deformation and that the eccentricity of Phobos has remained historically small.

We treat Phobos as a two-layered body made up of a homogeneous interior and a discrete incompressible outer layer. Surface stresses are computed using a thin-shell spherical approximation [*Sabadini and Vermeersen*, 2004; *Kattenhorn and Hurford*, 2009] (see Appendix B–Appendix D). The horizontal strain of this shell, as global shape evolves due to orbital decay, produces stresses on the surface given by

$$\sigma_{\theta\theta} = \frac{9M\mu_o h^2}{88\pi\rho_{av}}\left(\frac{1}{a_f^3}-\frac{1}{a_i^3}\right)(5+3\cos 2\theta) \quad (1)$$

$$\sigma_{\varphi\varphi} = -\frac{9M\mu_o h_2}{88\pi\rho_{av}}\left(\frac{1}{a_f^3}-\frac{1}{a_i^3}\right)(1-9\cos 2\theta) \quad (2)$$

where θ is the colatitude measured with respect to the axis through the center of the tidal bulge (i.e., $\theta = 0°$ corresponds to the sub-Mars point on Phobos' surface) [*Melosh*, 1977; *Leith and McKinnon*, 1996]. We define tension as positive and compression as negative. The surface stress $\sigma_{\theta\theta}$ is along the surface in the θ-direction, while $\sigma_{\varphi\varphi}$ is along the surface orthogonal to $\sigma_{\theta\theta}$. Here M is the mass of Mars, and a_i and a_f are the starting and final semimajor axes during any span of orbital decay.

The magnitude of the tidal stress on the surface is proportional to the displacement Love number h_2, which describes Phobos' tidal response. The value of h_2 depends on internal structure and material properties of our incompressible two-layer model (see Appendix B and Appendix D). Both layers have $\rho_{av} = 1880$ kg/m^3 and the total radius, R, is 11.1 km. The outer, stiffer layer is modeled as 100 m thick based on the thickness implied by the drainage of regolith into underlying cracks [*Horstman and Melosh*, 1989] or possibly into pore space in the interior.

The rigidities of the two layers are not well constrained. However, we assume that the inner layer is strong enough to support the overburden pressure, $\rho_{av} gR$, where g is the surface gravity, resulting in an overburden of ~10^5 Pa. The inner layer is conservatively modeled with a rigidity $\mu_i = 10^6$ Pa (see Discussion section). The outer layer is modeled with $\mu_o = 10^8$ Pa, based on the assumed regolith density and knowledge of S wave

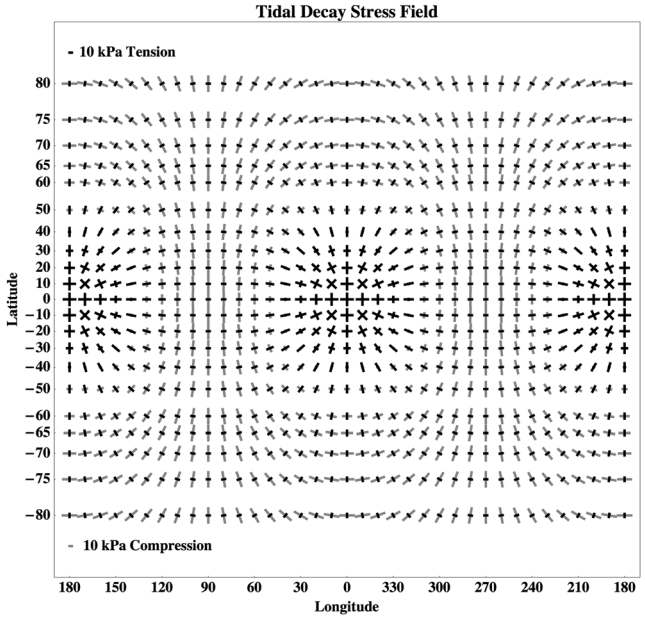

Figure 2. Stresses in a thin elastic shell computed for the last 10% of orbital decay for a spherical Phobos with a weak interior. The sub-/anti-Mars regions (centered at 0 and 180° longitude, respectively) experience tension in both principal stress directions. Over the rest of Phobos' surface, stresses radial to the tidal axis are tensile, while stresses concentric about the tidal axis are compressional. Tension fractures would tend to be concentric about the sub-/anti-Mars regions. Within the sub-/anti-Mars regions, the tensile stress is nearly isotropic near the tidal axis, and no preferred orientation is predicted.

velocities that are found to be uniformly ~200 m/s ($\mu = \rho v^2$) in Lunar regolith [*Horvath et al.*, 1980]. For these model parameters, $h_2 = 0.021$, which corresponds to a tidal bulge height of ~24 m at the sub-Mars point.

Figure 2 shows the stress field predicted on Phobos from orbital migration starting at 3 R_{Mars} to the current orbital radius (2.77 R_{Mars}). Tensile tidal stresses range from ~50 kPa near the sub-/anti-Mars regions to >10 kPa at points in between. In the sub-/anti-Mars regions, both principal stresses are tensile, whereas in the interbulge regions, stresses radial to the tidal axis are tensile and stresses concentric about the tidal axis are compressive. This pattern qualitatively fits the orientation of grooves on Phobos' surface.

Extension of work done on Mercury [*Melosh*, 1977] would predict strike-slip failure on Phobos due to the tidal stress if the outer layer tensile strength is sufficiently high. However, if tidal tension is comparable to or greater than the tensile strength of the surface layer, tensile failure that would produce fractures perpendicular to the tensile stress is a possible mode of failure [*Helfenstein and Parmentier*, 1983]. This type of surface failure has been extensively researched on icy satellites [*McEwen*, 1986; *Greenberg et al.*, 1998]. Moreover, experiments with material designed to simulate Lunar regolith suggest that tensile failure occurs at stresses as low as 1 kPa [*Arslan et al.*, 2008]. Therefore, we propose that the orbital decay tidal stress can drive tensile failure of the surface in a similar manner. This hypothesis means that the principal tensile stress should be normal to the grooves. To test this, we mapped ~200 of the most prominent linear surface features (Figure 3). Using the latitude, longitude, and strike for multiple points along these fractures, we calculated the principal tidal stress tensor experienced along each fracture in response to orbital decay. The principal stress tensor was then decomposed relative to the local strike of the fracture, yielding the normal stress across each fracture. The magnitudes of the computed stresses, as well as the correlation between principal stress orientations and the azimuths of observed fractures, provide the critical tests of the tidal fracturing model.

There is a strong correlation between the surface stress field and the geometry of Phobos' grooves (Figure 3). The majority of grooves (warmer colors in Figure 3) experience a tensile stress normal to their strikes, indicating that they could have formed (or are still forming) by tensile failure of the outer shell. Note that we do not model failure explicitly nor the stress perturbation associated with the opening of a fracture.

The orientations of most grooves on Phobos are closely aligned with the modeled tidal stress field. In regions of anisotropic horizontal stress, we expect the surface to fail perpendicular to the direction of maximum tension. Indeed, many of the grooves experiencing tension in these regions are aligned almost perfectly perpendicular to the direction of maximum tidal tensile stress (redder colors in Figure 3). In the sub-/anti-Mars equatorial regions, both principal stresses are tensile; however, failure will still occur perpendicular to the maximum tension as soon as the tensile strength of the surface layer is reached. Where the principal stresses have nearly equal magnitudes (i.e., approaching an isotropic stress field), no preferred formation orientation is predicted. Preferred fracture orientations in these regions are therefore less reliably compared to the tidal stress field (dark gray lines in Figure 3) and may be influenced by local sources of stress. For example, stresses

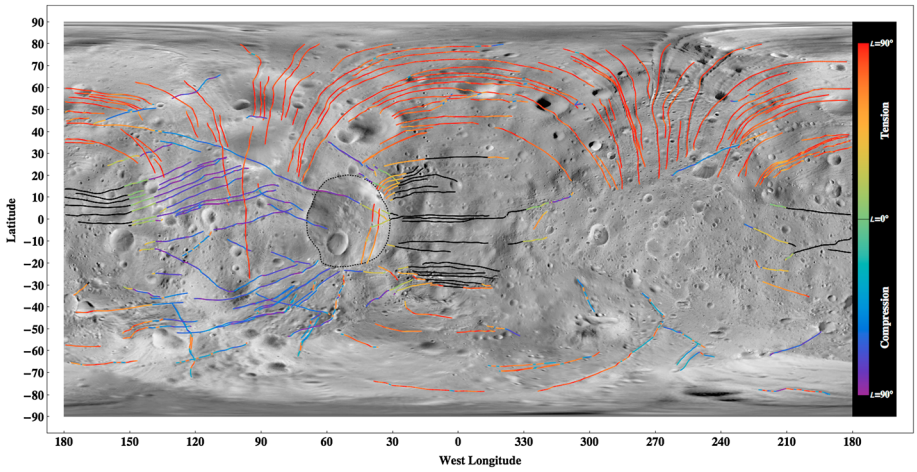

Figure 3. Locations and orientations of grooves mapped for this project. The orientation of each groove can be compared to the tidal principal stress field to assess goodness of fit to the principal tension direction. A majority of the observed fractures experience tensile stress normal to their strike (warmer colors), while a cluster of fractures in the leading hemisphere are oriented such that the normal stress would be compressional across them (cooler colors). Most fractures in tension, and in regions with clear large asymmetry in principal stresses, are aligned nearly perfectly with the principal stresses; i.e., the principal tensile stress is perpendicular to the fracture (redder colors). The orientation fits of fractures in the sub-/anti-Mars regions (gray) are difficult to assess since the tidal stress is almost isotropically tensile. Any preferred formation orientations in these areas may be influenced by local stress anisotropy (e.g., Stickney crater, outlined for clarity).

from the impact that produced Stickney could have combined with tidal stresses to preferentially produce east-west grooves in the sub-Mars region near Stickney crater or if the grooves postdate Stickney, topography of the crater may have influenced the surface stress concentration.

3. Discussion

There is a relative paucity of tidally aligned grooves S and SE of the sub-Mars point. This might be attributed to the absence of a cohesive material in this location (e.g., coarser regolith [*Scheeres et al.*, 2010]). Limited spectroscopy data show regional compositional differences that might correspond to varying regolith elastic properties [*Witasse et al.*, 2014; *Rivkin et al.*, 2002]. Nonaligned grooves are not random (cooler colors in Figure 3) but cluster in the equatorial zones between the sub-/anti-Mars tidal bulges; they require an alternative or additional explanation for their formation. Considering that the predominant formation orientations are at high angles to the maximum compression direction, such grooves could represent contractional failure of surface materials. Alternatively, they may have formed under different stress conditions, such as the stresses produced when Phobos experienced nonsynchronous rotation before becoming tidally locked [*Weidenschilling*, 1979]. They are found predominantly in the orbital leading hemisphere, which might also allow for their formation by sweep up of coorbiting material derived from Phobos, Deimos, or even Mars [*Murray and Heggie*, 2014].

Morphologically, grooves resemble extensional tectonic features. The majority of grooves form remarkably linear, consistent topographic depressions in distinct sets. Groove widths and spacings are relatively homogeneous, as is typical of extensional fracture sets in a uniform thickness brittle layer. Scalloped edges along many grooves are consistent with pit chain morphologic evolution, whereby initially isolated pits merge along strike to create a continuous feature, as is described across the solar system [*Horstman and Melosh*, 1989; *Ferrill et al.*, 2004; *Wyrick et al.*, 2004; *Nahm and Kattenhorn*, 2015]. Initially isolated pits in loose regolith align above an underlying dilational crack, into which regolith progressively drains. The circular edges of the original pits create the scalloped margin effect, although linear margins may also develop if the underlying structure is a dilational fault or graben [e.g., *Ferrill et al.*, 2004; *Grant and Kattenhorn*, 2004]. Bright margins along shadowed edges of some grooves imply upturned flanks, which can be produced by footwall uplift along normal faults. Inferred extensional deformation thus justifies comparisons to the principal extension direction to determine the viability of an orbital decay driving mechanism.

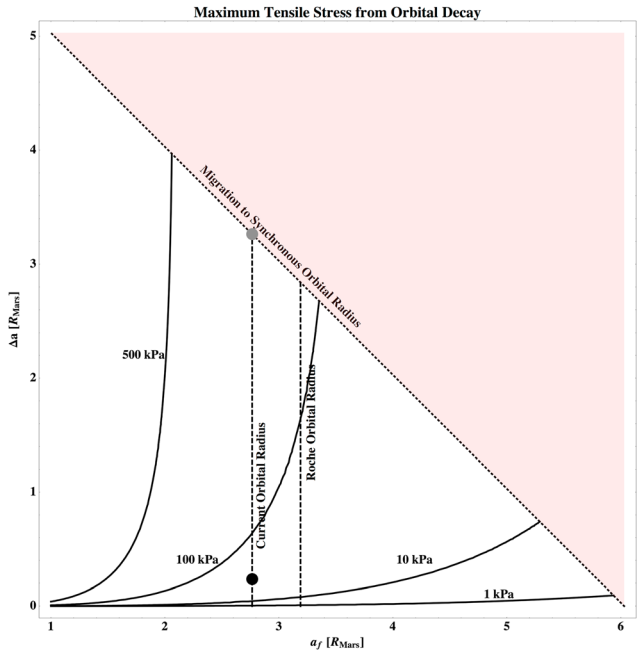

Figure 4. The maximum tensile stress experienced on Phobos for various amounts of orbital decay toward an orbital distance a_f and for a change in orbital distance Δa. Earlier in Phobos' orbital history, significant stresses could be generated, allowing multiple generations of fractures to evolve on its surface with ongoing orbital decay over time. The black dot represents the case illustrated in the text for which migration starts (a_i) at an orbital radius of 3.0 R_{Mars} and ends at the current orbital radius ($a_f = 2.77\ R_{Mars}$; $\Delta a = 0.23$), resulting in a maximum tensile stress of ~50 kPa. The gray dot represents the maximum stress that could be generated if Phobos migrated from the synchronous orbital radius, which results in >100 kPa of stress.

Where two or more crosscutting sets with disparate orientations exist (Figure 3), multiple stages of tectonic extension and direction are implied. In such cases, relative ages of groove sets can be determined either by direct evidence of crosscutting relationships or by their ages relative to craters that formed intermediate to the two groove sets. For example, some of the ENE oriented groove sets west of Stickney (cooler colors in Figure 3) have pit chain morphologies that imply that they formed in extension, despite currently experiencing compression in the contemporary orbital decay stress field. Moreover, they are older than the N-S grooves in the same region that show a strong correlation to the orbital decay stress field. These relationships are observed elsewhere across Phobos. Hence, orbital decay is likely to be the key driving force behind the most recent Phobos deformation. Older extensional features imply that ancient stress fields differed from that produced spatially by orbital decay today, perhaps explaining mismatches (purple grooves) in Figure 3. In rare cases (e.g., the NW oriented groove projecting NW away from Stickney crater), linear features show less resemblance to pit chains and may be catenae (aligned impact craters). In such cases, the pits (craters) vary in size and spacing and are typically larger than pits caused by the draining of regolith. The catena mentioned above almost encircles Phobos, creating a sinusoidal trace across the surface in the fracture map (Figure 3) and predates the youngest tectonic grooves.

Orbital decay from 3.0 to 2.77 R_{Mars} can produce ~50 kPa of tensile stress at the sub-/anti-Mars point (Figure 4; the 0° longitude and 0° latitude point in Figure 2). While these stresses may seem low, experiments with Lunar simulant suggest that tensile failure occurs at stresses as low as 1 kPa [*Arslan et al.*, 2008]. We find that stresses from orbital decay are up to 50 times larger, making deep groove formation plausible by our proposed mechanism and high enough to drive fractures to depths of up to 5 km, thus providing a mechanism to create dilational cracks below the surface layer into which regolith may have drained to form surface pit chains.

These stress levels were theoretically achievable early in the history of Phobos' ongoing orbital decay (Figure 4), so in principle, there could be generations of fractures and a range of evolutionary morphologies. Hence, grooves do not all have to be young according to our model, consistent with the apparent protracted history of their formation [*Weidenschilling*, 1979]. As successive generations of grooves form, their pattern of orientations should remain relatively consistent over time as long as Phobos' tidal alignment with Mars remains constant. Impact events might break the tidal alignment occasionally, but Phobos' irregular shape presumably helps to quickly reestablish a tidally spin-locked system.

While the bulk rigidity (μ_B) of Phobos is not constrained, the bulk rigidity for the nominal model presented here for Phobos is ~10^6 Pa. This value is lower than the lower bound estimate for Phobos' rigidity of 5×10^8 Pa [*Yoder*, 1982]. Surveys of 1 km class asteroid binaries have observed asteroids with rigidities ranging from 10^5 Pa to 10^8 Pa with a median value of ~5×10^6 Pa [*Taylor and Margot*, 2011], assuming the tidal quality factor for dissipation (Q) is similar to rocky bodies, Q~100. If Phobos behaves like these smaller asteroids, it is plausible that its bulk rigidity can be ~10^6 Pa. However, larger 100 km class binaries were found to be more rigid, ranging from 10^7 Pa to 10^{13} Pa with

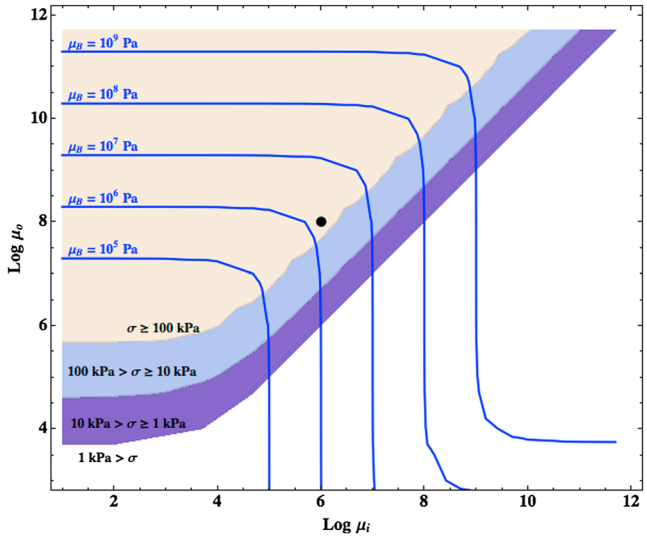

Figure 5. The nominal rigidity model for Phobos, adopted in this paper, provides stresses above 100 kPa for migration from ~6 R_{Mars} to the current orbital radius (gray dot in Figure 4). This model is not unique and a variety of combinations of models with inner layer rigidity (μ_i) and outer layer rigidity (μ_o) can produce the stress in excess of 100 kPa, when two-layer modes with the indicated rigidity values are evaluated (see Appendix B and Appendix C). Our nominal model produces a bulk rigidity (μ_B) of ~10^6 Pa.

a median value of ~10^9 Pa (again assuming $Q = 100$) [*Taylor and Margot*, 2011], but these bodies are gravity dominated and Phobos' size places it at transition point between strength and gravity-dominated bodies [*Asphaug et al.*, 2015]; therefore, we posit that its rigidity could be similar to the 1 km class asteroids.

A finding that Phobos' interior is weak is consistent with hypothesized formation scenarios. If Phobos was formed by the accretion of debris in Martian orbit, resulting from a large impact [*Citron et al.*, 2015], then the process of moon building may have resulted in Phobos being inherently weak, with a core similar to a rubble pile. Predictions of the rigidity of a 10 km rubble pile yield values ~10^7 Pa [*Goldreich and Sari*, 2009], which are only an order of magnitude stronger than the model in this study. Regardless, the tidal model for fracture formation can still produce large stresses on Phobos for other assumptions of layer rigidities (Figure 5).

Our assumption that the outer layer is 100 m thick is a conservative upper limit, as the estimated thickness of the regolith varies from 5 to 100 m [*Basilevsky et al.*, 2014]. The effect of thinner shells is explored in Appendix D and in general results in higher levels of stress. Therefore, we find that our results are robust and are valid even if future investigations of Phobos can place different constraints on some of the values we assume for Phobos' interior properties. Once fractures have been formed on Phobos' surface, they can remain active through diurnal tidally driven motions. Phobos' orbital eccentricity produces a dynamic diurnal stress field, which changes throughout Phobos' 7.6 h orbit. While these stresses are smaller by an order of magnitude, they can still work to dilate the grooves similar to the tidal dilation of fractures on Enceladus [*Hurford et al.*, 2007]. The reworking of fractures by these stresses may be natural seismic sources [*Lee et al.*, 2003], which could be exploited by future missions to probe Phobos' interior. However, Phobos quakes are only possible if the interior is weak, allowing an enhancement of tidal diurnal stress. Thus, a seismometer could quickly determine the state of Phobos' interior; it would be rigid if there are no quakes on the diurnal time scale, and weak if there are quakes. Furthermore, Phobos quakes would allow a natural way to probe the properties of Phobos' internal structure.

The presence of tidally driven fracturing on Phobos does not imply its imminent catastrophic disruption, particularly given that a friction angle of only ~3° is sufficient to prevent downslope movement today, even in the complete absence of cohesion [*Holsapple*, 2001]. Tidal disaggregation of Phobos will occur only when it is much closer to Mars and is suggested to occur in 20–40 Ma [*Black and Mittal*, 2015]. But meanwhile, Phobos is weak enough internally, on the time scale of orbital migration, to permit global deformation that results in stresses to build up within an elastic lunar-like outer layer. According to our model, its failure is opening up granular fissures, an interpretation that is consistent with the hypothesis that the pitted grooves are formed by regolith draining into fractures [*Horstman and Melosh*, 1989].

4. Conclusions

Our model results applied to surface observations imply that Phobos is a rubble pile overlain by a lunar-like cohesive regolith layer. This layer is developing extensional fissures as the global body deforms in response to increasing tides related to orbital decay. More detailed study by an orbiter or lander will provide better

constraints on the satellite's geologic evolution, and its suitability for human exploration given what may be an active and evolving surface.

5. Appendices

The following material serves as a reference for the reader. In general, it provides more detailed information that is supplemental to the main text. In particular the sections detail the following:

Reviews the problem of assuming that Phobos is a homogeneous sphere when determining tidal stresses on its surface. This finding has not been well preserved in the literature.
Details how the tidal deformation of a two-layer model is determined. The standard theory here can provide the Love number h_2.
Details the extension of the two-layer model in Appendix B to determine the stresses on the surface of the sphere. This method is not well documented in the literature.
Discusses the evaluation of stress on the surface given by the two-layer model. It also shows how robust and sensitive the results are to model parameters. Finally, it demonstrates that a thin-shell model can approximate stresses on the surface for our nominal model parameters. Because the thin-shell equations are straightforward, we adopt them for the main text but this material serves as justification for that simplification.

Appendix A: Tidal Stress on a Homogeneous Sphere

Surface stresses on a homogeneous sphere due to orbital migration are given by

$$\sigma_{\theta\theta} = \frac{9M\mu h^2}{20\pi\rho_{av}}\left(\frac{1}{a_f^3} - \frac{1}{a_i^3}\right) \tag{A1}$$

$$\sigma_{\varphi\varphi} = -\frac{9M\mu h_2}{40\pi\rho_{av}}\left(\frac{1}{a_f^3} - \frac{1}{a_i^3}\right)(1 - 3\cos 2\theta) \tag{A2}$$

where θ is the colatitude measured with respect to the axis through the center of the tidal bulge [*Kattenhorn and Hurford*, 2009]. Tension is positive and compression negative. The surface stress $\sigma_{\theta\theta}$ is along the surface in the θ direction, while $\sigma_{\varphi\varphi}$ is along the surface orthogonal to $\sigma_{\theta\theta}$. Surface radial and shear stresses are required to be zero. Here M is the mass of Mars, μ is the rigidity, and a_i and a_f are the initial and final semimajor axes during orbital decay. The average density of Phobos is given by ρ_{av}, while its second-order tidal surface displacement Love number h_2 is given by the classical solution [*Love*, 1911],

$$h_2 = \frac{5/2}{\frac{19\mu}{2\rho_{av}gR} + 1}, \tag{A3}$$

where g is the surface gravity of Phobos and R is the average radius.

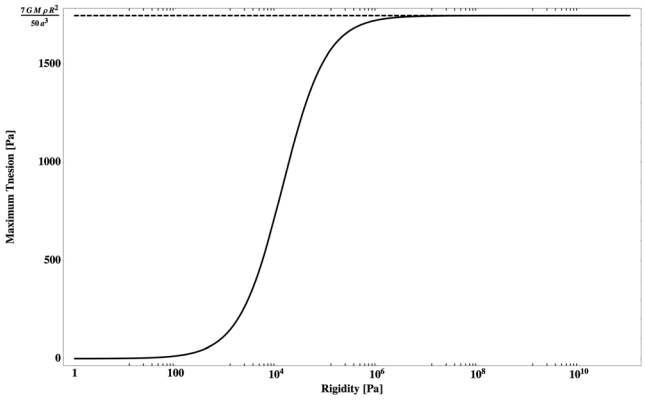

Figure A1. Maximum tensile stress on the surface of a homogenous Phobos depends on the assumed value of its rigidity. For a rigid Phobos, the stress increases to a limit of $\frac{7GM\rho_{av}R^2}{50a^3}$, which for the parameters adopted in this study would yield about 1700 Pa.

In the homogeneous solution, surface stress $\sigma_{\theta\theta}$ is constant and always tensile, while surface stress $\sigma_{\varphi\varphi}$ is tensile in the sub-/anti-Mars regions, extending to angular distances of 35.3° and compressive elsewhere. Tidal stresses are maximized as $a_i \rightarrow \sim \frac{11}{5} a_f$, representing the tidal deformation from a sphere to the current tidal shape. In the case that Phobos is dominated by its material strength (i.e., $\frac{19\mu}{2\rho_{av}gR} \gg 1$), the maximum tensile stresses go to a limiting value of $\sim \frac{7GM\rho_{av}R^2}{50a^3}$, which for the parameters adopted in this study would yield about 1700 Pa (1.7 kPa). These stresses, although of the correct orientation for grooves, are not likely of a high enough

magnitude for groove formation. Decreasing the rigidity of the homogenous Phobos allows greater tidal deformation but will not result in the production of greater stresses (Figure A1).

Appendix B: Two-Layer Model of Tidal Deformation

In order to find a solution for the tidal deformation of an incompressible spherical two-layer body, we follow the derivation of *Sabadini and Vermeersen* [2004]. In this method, six coupled differential equations are solved simultaneously to find the equilibrium tidal deformation. The six differential equations solve for two displacements, u_r and u_θ, two stresses, σ_{rr} and $\sigma_{r\theta}$, the tide-raising potential, V, and the continuity of the tidal potential, q (sometimes called the potential stress), at the top of each layer. These six equations can be written, to second order, in the following forms as

$$u_r = \eta y_1 R^2 P_2(\cos\theta), \tag{B1}$$

$$u_\theta = \eta y_2 R^2 S_2(\cos\theta), \tag{B2}$$

$$\sigma_{rr} = \eta y_3 R^2 P_2(\cos\theta), \tag{B3}$$

$$\sigma_{r\theta} = \eta y_4 R^2 S_2(\cos\theta), \tag{B4}$$

$$V = \eta y_5 R^2 P_2(\cos\theta), \text{ and} \tag{B5}$$

$$q = \eta y_6 R^2 P_2(\cos\theta). \tag{B6}$$

In these equations, $\eta = \frac{GM}{a^3}$ with a the orbital radius and G the gravitational constant. R is the average radius of Phobos and $S_2(\cos\theta)$ is the derivative of $P_2(\cos\theta)$, the second-order Legendre polynomial with respect to θ. The six functions (y_1, y_2, y_3, y_4, y_5, and y_6) shown here all have the same form in that each of the terms is linear in the constants of integration such that

$$\vec{y_i} = Y(u,\rho,g,r)\,\vec{A} \tag{B7}$$

where $Y(\mu,\rho,g,r)$ is the matrix of functions that describe the y_i equations in terms of the constants of integration, $\vec{A}$. As noted in *Sabadini and Vermeersen* [2004], the $Y(\mu,\rho,g,r)$ matrix for spherical harmonic degree-2 is given by

$$Y(\mu,\rho,g,r) = \begin{bmatrix} \frac{r^3}{7} & r & 0 & \frac{1}{2r^2} & \frac{1}{r^4} & 0 \\ \frac{5r^3}{42} & \frac{r}{2} & 0 & 0 & -\frac{1}{3r^4} & 0 \\ \frac{1}{7}r^2(-\mu+\rho g r) & 2\mu+\rho g r & -\rho r^2 & \frac{-6\mu+\rho g r}{2r^3} & \frac{-8\mu+\rho g r}{r^2} & -\frac{\rho}{r^3} \\ \frac{8\mu r^2}{21} & \mu & 0 & \frac{\mu}{2r^3} & \frac{8\mu}{3r^5} & 0 \\ 0 & 0 & -r^2 & 0 & 0 & -\frac{1}{r^3} \\ \frac{3}{7}\gamma\rho r^3 & 3\gamma\rho r & -5r & \frac{3\gamma\rho}{2r^2} & \frac{3\gamma\rho}{r^4} & 0 \end{bmatrix} \tag{B8}$$

where $\gamma = \frac{4}{3}\pi G$.

The value of $\vec{y_i}$ at any radius can be found, if the constants of integration are known, by evaluating Y at that radius. In this case, we do not know $\vec{A}$. So we next describe an alternative way of finding $\vec{y_i}$ based on knowing their values at a different radius. The propagator matrix P is defined such that it gives $\vec{y_i}$ at $r = R_2$ based on values at $r = R_1$:

$$\vec{y_i}\,(r_2) = P(\mu,\rho,g_1,g_2,R_1,R_2)\,\vec{y_i}\,(r_1) \tag{B9}$$

P is known as the "propagator" matrix. This matrix translates the solution radially within a layer in which the material properties are constant. This will allow the propagation of boundary conditions from one layer boundary to the next. The propagator matrix can be expressed in terms of $Y(\mu,\rho,g,r)$:

$$P(\mu,\rho,g_1,g_2,R_1,R_2) = Y(\mu,\rho,g_2,R_2)\,Y^{-1}(\mu,\rho,g_1,R_1) \tag{B10}$$

At $r = 0$, the solution must be finite, yet there are three irregular solutions which approach infinity at this limit, allowing us to reduce the solution to three constants of integration just as Love did for a uniform sphere [*Arslan et al.*, 2008]. Therefore, the values of $\vec{y_i}$ in the inner layer depend on only three constants of integration, and the matrix equation is reduced to

$$\vec{y_i}\ (\mu_1, \rho_1, g_1, r) = Y(\mu_1, \rho_1, g_1, r) I_1\ \vec{A_1} \tag{B11}$$

for $r < R_1$, where $\vec{A_1}$ is a vector of the constants of integration for the inner layer, and

$$I_1 \equiv \begin{bmatrix} 1 & 0 & 0 \\ 0 & 1 & 0 \\ 0 & 0 & 1 \\ 0 & 0 & 0 \\ 0 & 0 & 0 \\ 0 & 0 & 0 \end{bmatrix}. \tag{B12}$$

In the model, the continuity of the material requires that the displacement and potential (and thus the $\vec{y_i}$) must be continuous across the layer boundaries. This continuity means that at the inner layer/outer layer boundary

$$\vec{y_i}\ (\mu_1, \rho_1, g_1, R_1) = \vec{y_i}\ (\mu_2, \rho_2, g_2, R_1). \tag{B13}$$

Next consider the outer layer. The solution anywhere in the layer ($R_1 < r < R_2$) can also be given by $\vec{y_i}\ (\mu_2, \rho_2, g_2, r) = P(\mu_2, \rho_2, g_1, g_2, R_1, r)\ \vec{y_i}\ (\mu_2, \rho_2, g_2, R_1)$ if the solution at $r = R_1$ is known. However, using the continuity of the solution across the boundary, the solution anywhere in this layer can also be described using the solution for the inner layer, $\vec{y_i}\ (\mu_2, \rho_2, g_2, r) = P(\mu_2, \rho_2, g_1, g_2, R_1, r)\ \vec{y_i}\ (\mu_1, \rho_1, g_1, R_1)$ which now depends only on the three constants of integration from the inner layer. By letting $r = R_2$, the solution at the surface is described in terms of three constants of integration. The solution from the inner layer/outer layer boundary at $r = R_1$ is said to have been "propagated" to the surface.

Now the boundary conditions at the surface can be applied in order to find the three constants of integration. These boundary conditions are the same as for a uniform sphere. The outer surface is stress free ($y_3 = 0$ and $y_4 = 0$). Also, there is continuity in the potential across the outer surface ($y_6 = 5/R_2$). Setting up the matrix equation to match the boundary conditions gives

$$I_2 P(\mu_2, \rho_2, g_1, g_2, R_1, R_2) Y(\mu_1, \rho_1, g_1, R_1) I_1\ \vec{A_1} = \vec{b} \tag{B14}$$

where $\vec{b}$ is the vector of the boundary conditions on y_3, y_4, and y_6, respectively,

$$\vec{b} = \begin{bmatrix} 0 \\ 0 \\ 5/R_2 \end{bmatrix} \tag{B15}$$

and I_2 is a matrix that selects only the y_3, y_4, and y_6 solutions,

$$I_2 \equiv \begin{bmatrix} 0 & 0 & 1 & 0 & 0 & 0 \\ 0 & 0 & 0 & 1 & 0 & 0 \\ 0 & 0 & 0 & 0 & 0 & 1 \end{bmatrix}. \tag{B16}$$

Solving equation (B14) yields $\vec{A_1}$, the set of three constants of integration

$$\vec{A_1} = [I_2 P(\mu_2, \rho_2, g_1, g_2, R_1, R_2) Y(\mu_1, \rho_1, g_1, R_1) I_1]^{-1}\ \vec{b}\ . \tag{B17}$$

Once the constants of integration are known, the $\vec{y_i}$ at the surface can be fully described. The tidal response of the two-layer body as given by h_2 is related to y_1 as follows:

$$h_2 = y_1 g_2 \tag{B18}$$

where g_2 is the acceleration of gravity at the surface (the top of the second layer).

Appendix C: Tidal Stress on the Surface of a Two-Layer Model

Even though a full solution has been found based on this propagation technique, sometimes it is useful to know the values of the six constants of integration at the surface of the outer layer. These six constants can be found by solving for them using the solution at the surface,

$$\vec{A_2} = Y^{-1}(\mu_2,\rho_2,g_2,R_2)P(\mu_2,\rho_2,g_1,g_2,R_1,R_2)Y(\mu_1,\rho_1,g_1,R_1)I_1\ \vec{A_1} \tag{C1}$$

This will be especially useful for calculating the surface stresses, which are given by the equations

$$\sigma_{\theta\theta} = \eta R^2[y_7 P_2(\cos\theta) + y_8 S_2(\cos\theta)]\text{and} \tag{C2}$$

$$\sigma_{\varphi\varphi} = \eta R^2[y_7 P_2(\cos\theta) + y_8 T_2(\cos\theta)] \tag{C3}$$

where $T_2(\cos\theta)$ is the derivative of $P_2(\cos\theta)$ with respect to θ multiplied by $\cot\theta$. The new functions y_7 and y_8 are similar to the y_i functions in that they depend on the same constants of integration. These functions can be written in terms similar to the other functions and are

$$Y'(\mu,\rho,g,r) = \begin{bmatrix} \frac{1}{7}r^2(-5\mu+\rho g r) & 2\mu+\rho g r & -\rho r^2 & \frac{\rho g}{2r^2} & \frac{2\mu+\rho g r}{r^5} & -\frac{\rho}{r^3} \\ \frac{5\mu r^2}{21} & \mu & 0 & 0 & -\frac{2\mu}{3r^5} & 0 \end{bmatrix}. \tag{C4}$$

Thus, the y'_i functions can be evaluated by

$$\vec{y'_i}\ (\mu_2,\rho_2,g_2,R_2) = Y'(\mu_2,\rho_2,g_2,R_2)\ \vec{A_2}\ . \tag{C5}$$

The stress from orbital migration can be found as $\sigma_{\theta\theta}$ and $\sigma_{\varphi\varphi}$ change due to the change in orbital distance, i.e., evaluating η with a specific value of a,

$$\Delta\sigma_{\theta\theta} = \sigma_{\theta\theta}(a_f) - \sigma_{\theta\theta}(a_i)\text{and} \tag{C6}$$

$$\Delta\sigma_{\varphi\varphi} = \sigma_{\varphi\varphi}(a_f) - \sigma_{\varphi\varphi}(a_i). \tag{C7}$$

The tidal tensile stresses are maximized under the conditions that $a_i \rightarrow \tilde{} \frac{11}{5} a_f$ at $\theta = 0$, the sub/anti-Mars point.

Appendix D: Evaluation of a Two-Layer Phobos Model

We use the incompressible two-layer model (Appendix B) to evaluate the tidal response for Phobos. The model is built of an inner layer with material properties of density ρ_1 and rigidity μ_1 with a radial extent of R_1. The outer layer has its own material properties of density ρ_2 and rigidity μ_2, but its outer radius is constrained to the average radius of Phobos, $R_2 = 11{,}200$ m. The model can have up to five free parameters. However, to simplify things, we assume that the density within the two layers is constant and set it to Phobos' average density, i.e., $\rho_1 = \rho_2 = 1880\ \text{kg/m}^3$. The model has now been reduced to three free parameters, and we further assume the rigidity of the outer layer to be 10^8 Pa, i.e., $\mu_2 = 1 \times 10^8$ Pa, based on an analog to the Lunar regolith layer [*Horvath et al.*, 1980]. We then can see how the stresses on the surface vary based on the rigidity of the inner layer μ_1 and the thickness of the outer shell, H (see Table D1 and Figure D1).

We find that for interiors with rigidities $< 10^6$ Pa, the stresses on the surface are well characterized by the thin-shell approximation for thinner shell thicknesses ($H \leq 100$ m). In the case of an outer shell with a thickness of 100 m, the thin-shell approximation conservatively estimates the magnitude of stress but would produce grooves with similar orientation as long as the stresses are high enough to fracture the shell.

In the main text, we adopt a nominal model with $\mu_1 = 10^6$ Pa and an outer shell that is 100 m in thickness. The magnitude of the tidal stress is roughly inversely proportional to the shell thickness. If the outer shell thickness is 10 m, tidal stresses as shown in Figure 3 would be increased by about a factor of 10. Thus, we find that our nominal model is a conservative estimate for computing stresses on Phobos' surface.

Even though Phobos is not quite spherical (it is a triaxial ellipsoid with radii of 13.0 km × 11.4 km × 9.1 km), we find that the stresses produced by a spherical shell model have orientations that match the orientations of grooves on the surface (Figure 3 in the main text). Therefore, to first order, we maintain that this model can characterize stresses on Phobos due to orbital decay. Further refinements to the stress model should provide even better fits between tidal stress and observed groove orientations. Future work should focus in tidal stresses on a triaxial ellipsoid.

Table D1. Table of Two-Layer Model Results Compared to a Thin-Shell Approximation Based on the Two-Layer Tidal Deformation, h_2[a]

Internal Rigidity μ_1 (Pa)	Shell Thickness H (m)	Love Number h_2	Max Tension Two-Layer Model (Pa)	Max Tension Thin-Shell Model (Pa)	% Difference Between the Models
10	10	0.51	4,955,560	4,936,376	0.4
100	10	0.51	4,948,085	4,929,442	0.4
1,000	10	0.50	4,874,481	4,861,157	0.3
10,000	10	0.44	4,238,124	4,269,774	−0.7
100,000	10	0.20	1,756,866	1,927,555	−9.7
1.00E + 06	10	0.03	201,703	298,042	−47.8
1.00E + 07	10	0.003	17,847	31,563	−76.8
1.00E + 08	10	0.0003	1,746	3,175	−81.8
1.00E + 09	10	0.00003	174	318	−82.4
1.00E + 10	10	0.000003	17	32	−83.2
1.00E + 11	10	0.0000003	2	3	−91.1
10	50	0.12	1,199,983	1,177,008	1.9
100	50	0.12	1,199,555	1,176,614	1.9
1,000	50	0.12	1,195,296	1,172,688	1.9
10,000	50	0.12	1,154,230	1,134,824	1.7
100,000	50	0.09	854,785	857,908	−0.4
1.00E + 06	50	0.03	214,342	249,751	−16.5
1.00E + 07	50	0.003	19,197	30,970	−61.3
1.00E + 08	50	0.0003	1,746	3,175	−81.8
1.00E + 09	50	0.00003	171	318	−86.5
1.00E + 10	50	0.000003	15	32	−108.8
1.00E + 11	50	0.0000003	0	3	1299.5
10	100	0.062	625,595	602,042	3.8
100	100	0.062	625,481	601,939	3.8
1,000	100	0.062	624,344	600,911	3.8
10,000	100	0.061	613,185	590,829	3.6
100,000	100	0.052	519,391	505,952	2.6
1.00E + 06	*100*	*0.021*	*194,620*	*207,827*	*−6.8*
1.00E + 07	100	0.003	20,448	30,260	−48.0
1.00E + 08	100	0.0003	1,746	3,175	−81.8
1.00E + 09	100	0.00003	163	319	−95.9
1.00E + 10	100	0.000003	9	32	−252.6
1.00E + 11	100	0.0000003	−6	3	151.2

[a]The model evaluated consists of two layers, each with a density of 1880 kg/m^3. The rigidity of the inner layer is given in the table, while the outer layer has a rigidity of 10^8 Pa. The thickness of the outer shell (H) is provided in the table and the total radius is 11.2 km. The nominal model used in the text is italicized. Table results are for the case of that starts (a_i) at an orbital radius of ~6.0 R_{Mars} to the current orbital radius (a_f = 2.77 R_{Mars}).

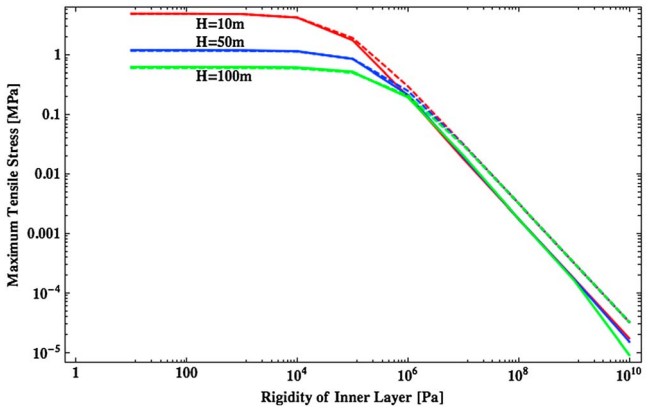

Figure D1. The maximum tensile stress on the surface of Phobos for various interior rigidities are shown for 2-layer models with three different outer shell thicknesses (10 m, 50 m and 100 m). The dashed lines show the thin-shell approximation for these stresses and are in good agreement with the two-layer result (solid line) as long as the interior's rigidity is $\leq 10^6$ Pa.

Acknowledgments

In general, this study is theoretical in nature, and numerical evaluations of the equations detailed herein were done for the parameters listed at locations on Phobos' surface determined by our mapping of surface features. While the figures provide a summary of our findings, both the data on our mapped fractures and numerical model results are available from the lead author upon request (terry.a.hurford@nasa.gov).

References

Arslan, H., S. Sture, and S. Batiste (2008), Experimental simulation of tensile behavior of lunar soil simulant JSC-1, *Mater. Sci. Eng. A*, *478*, 201–207.

Asphaug, E., G. Collins, and M. Jutzi (2015), *Global Scale Impacts, Chap. in Asteroids IV*, edited by P. Michel, Univ. of Arizona Press, Tucson, Ariz.

Basilevsky, A. T., C. A. Lorenz, T. V. Shingareva, J. H. Head, K. R. Ramsley, and A. E. Zubarev (2014), Surface geology and geomorphology of Phobos, *Planet. Space Sci.*, *102*, 95–118.

Bills, B. G., G. A. Neumann, D. E. Smith, and M. T. Zuber (2005), Improved estimate of tidal dissipation within Mars from MOLA observations of the shadow of Phobos, *J. Geophys. Res.*, *110*, E07004, doi:10.1029/2004JE002376.

Black, B. A., and T. Mittal (2015), The demise of Phobos and development of a Martian ring system, *Nat. Geosci.*, *8*, 913–917, doi:10.1038/ngeo2583.

Burns, J. A. (1978), The dynamical evolution and origin of the Martian moons, *Vista Astron.*, *22*, 193–210.

Citron, R. I., H. Genda, and S. Ida (2015), Formation of Phobos and Deimos via a giant impact, *Icarus*, *252*, 334–338.

Dobrovolskis, A. R. (1982), Internal stresses in PHOBOS and other triaxial bodies, *Icarus*, *52*, 136–148.

Ferrill, D. A., A. P. Morris, D. Y. Wyrick, D. W. Sims, and N. M. Franklin (2004), Dilational fault slip and pit chain formation on Mars, *GSA Today*, *14*(10), 4–12.

Goldreich, P., and R. Sari (2009), Tidal evolution of rubble piles, *Astrophys. J.*, *691*, 54–60.

Grant, J. A., and S. A. Kattenhorn (2004), Evolution of vertical faults at an extensional plate boundary, southwest Iceland, *J. Struct. Geol.*, *26*, 537–557.

Greenberg, G., P. Geissler, G. Hoppa, B. R. Tufts, and D. Durda (1998), Tectonic processes on Europa: Tidal stresses, mechanical response, and visible features, *Icarus*, *135*, 64–78.

Helfenstein, P., and E. M. Parmentier (1983), Patterns of fracture and tidal stresses on Europa, *Icarus*, *53*, 415–430.

Holsapple, K. A. (2001), Equilibrium configurations of solid cohesionless bodies, *Icarus*, *154*, 432–448.

Horstman, K. C., and H. J. Melosh (1989), Drainage pits in cohesionless materials: Implications for the surface of Phobos, *J. Geophys. Res.*, *94*, 12,433–12,441, doi:10.1029/JB094iB09p12433.

Horvath, P., G. V. Latham, Y. Nakamura, and H. J. Dorman (1980), Lunar near-surface shear wave velocities at the Apollo landing sites as inferred from spectral amplitude ratios, *J. Geophys. Res.*, *85*, 6572–6578, doi:10.1029/JB085iB11p06572.

Hurford, T. A., P. Helfenstein, G. V. Hoppa, R. Greenberg, and B. G. Bills (2007), Eruptions arising from tidally controlled periodic openings of rifts on Enceladus, *Nature*, *447*, 292–294.

Kattenhorn, S. A., and T. A. Hurford (2009), Tectonics of Europa, in *Europa*, pp. 199–236, The Univ. of Arizona Press, Tucson.

Kaula, W. M. (1964), *An Introduction to Planetary Physics: The Terrestrial Planets*, *Space Sci. Text Ser.*, Wiley, New York.

Lee, S., M. Zanolin, A. M. Thode, R. T. Pappalardo, and N. C. Makris (2003), Probing Europa's interior with natural sound sources, *Icarus*, *165*, 144–167.

Leith, A. C., and W. B. McKinnon (1996), Is there evidence for polar wander on Europa?, *Icarus*, *120*, 387–398.

Love, A. E. H. (1911), *Some Problems of Geodynamics*, Cambridge Univ. Press, Cambridge.

Lunine, J. I., G. Neugebauer, and B. M. Jakosky (1982), Infrared observations of PHOBOS and Deimos From Viking, *J. Geophys. Res.*, *87*, 10,297–10,305, doi:10.1029/JB087iB12p10297.

McEwen, A. (1986), Tidal reorientation and the fracturing of Jupiter's moon Europa, *Nature*, *321*, 49–51.

Melosh, H. J. (1977), Global tectonics of a despun planet, *Icarus*, *31*, 221–243.

Mignard, F. (1981), Evolution of the Martian satellites, *Mon. Not. R. Astron. Soc.*, *194*, 365–379.

Murray, J. B., and D. C. Heggie (2014), Character and origin of Phobos' grooves, *Planet. Space Sci.*, *102*, 119–143.

Nahm, A. L., and S. A. Kattenhorn (2015), A unified nomenclature for tectonic structures on the surface of Enceladus: Implications for Enceladus's tectonics and ice shell, *Icarus*, *258*, 67–81, doi:10.1016/j.icarus.2015.06.009.

Pieters, C. M., S. Murchie, N. Thomas, and D. Britt (2014), Composition of surface materials on the moons of Mars, *Planet. Space Sci.*, *102*, 144–151.

Rivkin, A. S., R. H. Brown, D. E. Trilling, J. F. Bell, and J. H. Plassmann (2002), Near-infrared spectrophotometry of Phobos and Deimos, *Icarus*, *156*, 64–75.

Sabadini, R., and B. Vermeersen (2004), *Global Dynamics of the Earth*, Kluwer Acad., Netherlands.

Scheeres, D. J., C. M. Hartzell, P. Sanchez, and M. Swift (2010), Scaling forces to asteroid surfaces: The role of cohesion, *Icarus*, *210*, 968–984.

Soter, S., and A. Harris (1977), Are striations on PHOBOS evidence for tidal stress, *Nature*, *268*, 421–422.

Taylor, P., and J.-L. Margot (2011), Binary asteroid systems: Tidal end states and estimates of material properties, *Icarus*, *212*, 661–676.

Thomas, P., J. Veverka, A. Bloom, and T. Duxbury (1979), Grooves on P–Phobos: Their distribution, morphology, and possible origin, *J. Geophys. Res.*, *84*, 8457–8477.

Weidenschilling, S. J. (1979), A possible origin for the grooves of Phobos, *Nature*, *282*, 697–698.

Willner, K., X. Shi, and J. Oberst (2014), Phobos' shape and topography models, *Planet. Space Sci.*, *102*, 51–59.

Wilson, L., and J. W. Head (1989), Dynamics of groove formation on Phobos by ejecta from Stickney, in *Proceedings of the 20th Annual Lunar and Planetary Science Conference*, pp. 1211–1212, Lunar Planet. Inst., Houston, Tex.

Witasse, O., et al. (2014), Mars express investigations of Phobos and Deimos, *Planet. Space Sci.*, *102*, 18–34.

Wyrick, D., D. A. Ferrill, A. P. Morris, S. L. Colton, and D. W. Sims (2004), Distribution, morphology, and origins of Martian pit crater chains, *J. Geophys. Res.*, *109*, E06005, doi:10.1029/2004/JE002240.

Yoder, C. F. (1982), Tidal rigidity of Phobos, *Icarus*, *49*, 327–346.